Synthetic simulations from a 2 1/2D model with real 3D topography

Stig Hestholm and Warren Ross, ExxonMobil Upstream Research Company

SUMMARY

Elastic and viscoelastic simulations have been pursued for a 2 1/2D model covered by a real 3D free surface topography. A 2D model has been extended into 2 1/2D to perform full 3D elastic and viscoelastic simulations. Seismograms and snapshots have been computed comparing free surface topography with the corresponding free plane surface simulations. Topography of only a very modest amount caused noticeable differences in the forward–scattered wavefield. We also compared viscoelasticity with elastic simulations, with and without topography. Q being very low for this example, the effect of viscoelasticity is to virtually eliminate the effect of modest topography. Nonetheless, small differences in amplitude still remain. For situations with higher Q or more pronounced elevation changes, incorporating topography is an important step in accurate surface–wave simulation and inversion.

INTRODUCTION

The free surface topography is the interface used in seismic modeling across which we encounter the most significant material property changes. Given this, along with the fact that elevation is among the best known data available, it should be accounted for in seismic modeling. In order to model free surface topography, various flavors on a few methods have been attempted. A tensorial formulation using irregular grids (Komatitsch et al., 1996) was used, as well as the more recently investigated spectral element method (Komatitsch et al., 1999, 2000). Its popularity is due to relatively high stability and dispersion bounds compared to other finite–element methods (Basabe and Sen, 2007), along with its inherent ability to exactly model free surfaces of any shapes due to its weak (integral) formulation of wave equations. For the same accuracy however, the computational cost is higher than using the finite–difference (FD) method, and this is all the more pronounced given the fact that up to 80% of the work during a simulation setup is typically dedicated to create the grid to represent the model necessary for the simulation. Such detailed representation of a model is unwarranted given that model interfaces of the subsurface are usually known only to within reflected P-wavelengths, which are increasing with depth.

Tessmer and Kosloff (1994); Tessmer et al. (1992) employ Chebyshev polynomials to discretize a wavefield formulation where the governing equations are transformed from a curved to a rectangular grid. The curved grid is automatically adapted to given surface topography elevation data and curvatures are gradually decreased with grid depth onto a plane surface at its bottom. Using this principle with FD discretization (Hestholm and Ruud, 1998; Hestholm, 1999), elastic and viscoelastic modeling were done with less cost and without any grid preparation procedure necessary for the spectral element method. Free-boundary conditions for surface topography (Hestholm and Ruud, 2002) were implemented at the upper model boundary, and no grid preparation is required for known surface elevation data.

We have pursued full 3D synthetic simulations for a 3D topography over a 2 1/2D medium derived from a real region, with and without topography, and using elastic and viscoelastic algorithms for corresponding simulations. Lower Q–values for P– and S–waves are used in the upper 50m of the viscoelastic simulations, which are based on time domain algorithms employing memory variables for time convolutions (Blanch et al., 1995; Carcione et al., 1988; Carcione, 1993).

GOVERNING EQUATIONS AND BOUNDARY CONDITIONS FOR 3D ELASTIC MEDIA

We introduce a linear mapping from a rectangular (ξ,κ,η)–grid to a curved grid in the (x,y,z)–system where both grids have positive direction upwards. The 3–D mapping can be written

$$x(\xi,\kappa,\eta)=\xi,\;\; y(\xi,\kappa,\eta)=\kappa,\;\; z(\xi,\kappa,\eta)=\frac{\eta}{\eta_{max}}z_0(\xi,\kappa). \quad (1)$$

$z_0(\xi,\kappa)$ is the topography function, and the rectangular (ξ,κ,η)–grid is bounded by $\xi=0$, $\xi=\xi_{max}$ and $\kappa=0$, $\kappa=\kappa_{max}$ horizontally and $\eta=0$ and $\eta=\eta_{max}$ vertically. The degree of stretching of the curved grid in the (x,y,z)–system is proportional to the height above the bottom plane ($z=0$). We assume the curved grid to be located in a Cartesian (x,y,z) coordinate system where the velocity–stress formulation of the seismic wave equations is valid. Then we transform the equations into the rectangular, computational (ξ,κ,η)–grid by using the chain rule and employing expressions for the partial derivatives of the coordinates (Hestholm, 1999),

$$\frac{\partial\xi}{\partial x}=1, \qquad \frac{\partial\xi}{\partial y}=0, \qquad \frac{\partial\xi}{\partial z}=0, \quad (2)$$

$$\frac{\partial\kappa}{\partial x}=0, \qquad \frac{\partial\kappa}{\partial y}=1, \qquad \frac{\partial\kappa}{\partial z}=0, \quad (3)$$

$$A=A(\xi,\kappa,\eta) \;\equiv\; \frac{\partial\eta}{\partial x}=-\frac{\eta}{z_0(\xi,\kappa)}\frac{\partial z_0(\xi,\kappa)}{\partial\xi}, \quad (4)$$

$$B=B(\xi,\kappa,\eta) \;\equiv\; \frac{\partial\eta}{\partial y}=-\frac{\eta}{z_0(\xi,\kappa)}\frac{\partial z_0(\xi,\kappa)}{\partial\kappa}, \quad (5)$$

$$C=C(\xi,\kappa) \;\equiv\; \frac{\partial\eta}{\partial z}=\frac{\eta_{max}}{z_0(\xi,\kappa)}. \quad (6)$$

We obtain the velocity–stress formulation of the elastic and viscoelastic wave equations in the rectangular (ξ,κ,η)–grid (Hestholm and Ruud, 1998; Hestholm, 1999), from which the elastic wave equations for stresses are

$$\frac{\partial\sigma_{xx}}{\partial t} = \Pi\left(\frac{\partial u}{\partial\xi}+A\frac{\partial u}{\partial\eta}+\frac{\partial v}{\partial\kappa}+B\frac{\partial v}{\partial\eta}+C\frac{\partial w}{\partial\eta}\right) -2\mu\left(\frac{\partial v}{\partial\kappa}+B\frac{\partial v}{\partial\eta}+C\frac{\partial w}{\partial\eta}\right), \quad (7)$$

$$\frac{\partial \sigma_{yy}}{\partial t} = \Pi\left(\frac{\partial u}{\partial \xi}+A\frac{\partial u}{\partial \eta}+\frac{\partial v}{\partial \kappa}+B\frac{\partial v}{\partial \eta}+C\frac{\partial w}{\partial \eta}\right) -2\mu\left(\frac{\partial u}{\partial \xi}+A\frac{\partial u}{\partial \eta}+C\frac{\partial w}{\partial \eta}\right), \quad (8)$$

$$\frac{\partial \sigma_{zz}}{\partial t} = \Pi\left(\frac{\partial u}{\partial \xi}+A\frac{\partial u}{\partial \eta}+\frac{\partial v}{\partial \kappa}+B\frac{\partial v}{\partial \eta}+C\frac{\partial w}{\partial \eta}\right) -2\mu\left(\frac{\partial u}{\partial \xi}+A\frac{\partial u}{\partial \eta}+\frac{\partial v}{\partial \kappa}+B\frac{\partial v}{\partial \eta}\right), \quad (9)$$

$$\frac{\partial \sigma_{xy}}{\partial t} = \mu\left(\frac{\partial u}{\partial \kappa}+B\frac{\partial u}{\partial \eta}+\frac{\partial v}{\partial \xi}+A\frac{\partial v}{\partial \eta}\right), \quad (10)$$

$$\frac{\partial \sigma_{xz}}{\partial t} = \mu\left(C\frac{\partial u}{\partial \eta}+\frac{\partial w}{\partial \xi}+A\frac{\partial w}{\partial \eta}\right), \quad (11)$$

$$\frac{\partial \sigma_{yz}}{\partial t} = \mu\left(C\frac{\partial v}{\partial \eta}+\frac{\partial w}{\partial \kappa}+B\frac{\partial w}{\partial \eta}\right), \quad (12)$$

which are needed in the derivation of the surface topography boundary conditions. Here ρ is the density, Π is the relaxation modulus for P–waves, $\Pi = \lambda + 2\mu$ (λ and μ are the Lamé parameters), and μ is the relaxation modulus for S–waves. The body forces are added in the momentum conservation equations (not shown here), u, v and w are the particle velocity components and σ_{xx}, σ_{yy}, σ_{zz}, σ_{xy}, σ_{xz} and σ_{yz} are the stress components. Together with the equations of motions these are the curved grid stress–strain relations governing wave propagation in a linear isotropic elastic medium. For viscoelasticity (Blanch et al., 1995), memory variables are added to equations (7)–(12), and additional equations are solved for them.

The boundary condition at any free surface is that the traction vector $\vec{T}$ vanishes, $\vec{T} \equiv \tau \cdot \vec{n} = 0$, i.e., in Cartesian coordinates, $\sigma_{ij} n_j = 0$, where τ is the stress tensor with components σ_{ij} and $\vec{n}$ is a normal vector to the local surface point with components n_j; $i, j = 1, 2, 3$. Any normal vector may be used, even though $\vec{T}$ is defined by the unit normal vector. In 3–D we can choose

$$\vec{n} = \left(-\frac{\partial z_0(\xi,\kappa)}{\partial \xi}, -\frac{\partial z_0(\xi,\kappa)}{\partial \kappa}, 1\right)^T = \left(-h_x, -h_y, 1\right)^T, \quad (13)$$

with $h_x = \partial z_0(\xi,\kappa)/\partial \xi$ and $h_y = \partial z_0(\xi,\kappa)/\partial \kappa$; h being the elevation data function and ^{T} means transposed. Partially differentiating the equations $\sigma_{ij} n_j = 0$ with respect to time and using the given $\vec{n}$ yields

$$-h_x\frac{\partial \sigma_{xx}}{\partial t} - h_y\frac{\partial \sigma_{xy}}{\partial t} + \frac{\partial \sigma_{xz}}{\partial t} = 0, \quad (14)$$

$$-h_x\frac{\partial \sigma_{xy}}{\partial t} - h_y\frac{\partial \sigma_{yy}}{\partial t} + \frac{\partial \sigma_{yz}}{\partial t} = 0, \quad (15)$$

$$-h_x\frac{\partial \sigma_{xz}}{\partial t} - h_y\frac{\partial \sigma_{yz}}{\partial t} + \frac{\partial \sigma_{zz}}{\partial t} = 0. \quad (16)$$

We now substitute the expressions for all time differentiated stresses from equations (7)–(12). Then equations (14)–(16) become

$$-h_x\Pi\left(\frac{\partial u}{\partial \xi}+A\frac{\partial u}{\partial \eta}\right) - h_x\lambda\left(\frac{\partial v}{\partial \kappa}+B\frac{\partial v}{\partial \eta}+C\frac{\partial w}{\partial \eta}\right) -h_y\mu\left(\frac{\partial v}{\partial \xi}+A\frac{\partial v}{\partial \eta}+\frac{\partial u}{\partial \kappa}+B\frac{\partial u}{\partial \eta}\right) +\mu\left(\frac{\partial w}{\partial \xi}+A\frac{\partial w}{\partial \eta}+C\frac{\partial u}{\partial \eta}\right) = 0, \quad (17)$$

$$-h_x\mu\left(\frac{\partial v}{\partial \xi}+A\frac{\partial v}{\partial \eta}+\frac{\partial u}{\partial \kappa}+B\frac{\partial u}{\partial \eta}\right) -h_y\lambda\left(\frac{\partial u}{\partial \xi}+A\frac{\partial u}{\partial \eta}+C\frac{\partial w}{\partial \eta}\right) - h_y\Pi\left(\frac{\partial v}{\partial \kappa}+B\frac{\partial v}{\partial \eta}\right) +\mu\left(\frac{\partial w}{\partial \kappa}+B\frac{\partial w}{\partial \eta}+C\frac{\partial v}{\partial \eta}\right) = 0, \quad (18)$$

$$-h_x\mu\left(\frac{\partial w}{\partial \xi}+A\frac{\partial w}{\partial \eta}+C\frac{\partial u}{\partial \eta}\right) - h_y\mu\left(\frac{\partial w}{\partial \kappa}+B\frac{\partial w}{\partial \eta}+C\frac{\partial v}{\partial \eta}\right) +\lambda\left(\frac{\partial u}{\partial \xi}+A\frac{\partial u}{\partial \eta}+\frac{\partial v}{\partial \kappa}+B\frac{\partial v}{\partial \eta}\right)+\Pi C\frac{\partial w}{\partial \eta} = 0. \quad (19)$$

Using the properties from equations (4)–(6) valid at the surface, $A = -Ch_x$ and $B = -Ch_y$, and rearranging terms give the following form of equations (17)–(19),

$$\begin{aligned} &\left[h_x^2\Pi + \mu\left(1+h_y^2\right)\right]C\frac{\partial u}{\partial \eta} + h_x h_y(\lambda+\mu)C\frac{\partial v}{\partial \eta} \\ &-h_x(\lambda+\mu)C\frac{\partial w}{\partial \eta} \\ =\ & h_x\Pi\frac{\partial u}{\partial \xi} + h_y\mu\frac{\partial v}{\partial \xi} - \mu\frac{\partial w}{\partial \xi} + h_y\mu\frac{\partial u}{\partial \kappa} + h_x\lambda\frac{\partial v}{\partial \kappa} \quad (20) \\ &h_x h_y(\lambda+\mu)C\frac{\partial u}{\partial \eta} + \left[\mu\left(1+h_x^2\right)+h_y^2\Pi\right]C\frac{\partial v}{\partial \eta} \\ &-h_y(\lambda+\mu)C\frac{\partial w}{\partial \eta} \\ =\ & h_y\lambda\frac{\partial u}{\partial \xi} + h_x\mu\frac{\partial v}{\partial \xi} + h_x\mu\frac{\partial u}{\partial \kappa} + h_y\Pi\frac{\partial v}{\partial \kappa} - \mu\frac{\partial w}{\partial \kappa} \quad (21) \\ &-h_x(\lambda+\mu)C\frac{\partial u}{\partial \eta} - h_y(\lambda+\mu)C\frac{\partial v}{\partial \eta} \\ &+\left[\Pi+\mu\left(h_x^2+h_y^2\right)\right]C\frac{\partial w}{\partial \eta} \\ =\ & -\lambda\frac{\partial u}{\partial \xi} + h_x\mu\frac{\partial w}{\partial \xi} - \lambda\frac{\partial v}{\partial \kappa} + h_y\mu\frac{\partial w}{\partial \kappa}. \quad (22) \end{aligned}$$

Equations (20)–(22) are exact 3–D boundary conditions for an arbitrary, smooth, free surface topography. They are discretized by second–order centered staggered FD operators. Near the free surface, gradually decreased order of centered staggered FD methods are used (Fornberg, 1988), while staggered 8th order FDs are employed in the interior of the domain (Kindelan et al., 1990; Holberg, 1987). The exponential damping method of Cerjan et al. (1985) is applied within absorbing strips at the sides and bottom of the computational domain, together with viscoelastic damping (low Q).

SIMULATIONS FROM A REAL REGION

A real 3D topography and a 2D subsurface model is chosen for all seismic simulations, extending the 2D model to 2 1/2D. The 2D section is 1250m long in the x-direction and 350m deep. It is extended to 200m in the y-direction and discretized by a grid sampling of 1m. Lee and Ross (2008) describe in some detail the derivation of this model. Due to the 200m

Synthetic topography simulations

absorbing boundaries at the ends and bottom, the medium is effectively 850m long in the x-direction and 150m deep. Only 40m absorbing strips are used in the y-direction, to make the effective model length in the y-direction to be 120m. Figure 1 is the cross-section of the S–wave velocities, which are as low as 184 m/s near the surface. P–velocities range up to around 2600 m/s.

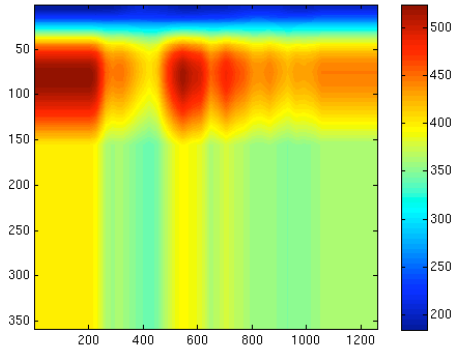

Figure 1: S-velocity of 2D cross-section.

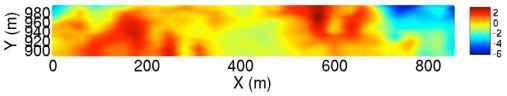

Figure 2: Surface view of real 3D topography used.

A Ricker P-wave source with 10 Hz central frequency is inserted at $x = 325$m, $y = 100$m, at 5m depth. We will compare snapshots and seismograms for four different scenarios using the 2 1/2D model of cross section of Figure 1 and real free surface topography of Figure 2: 1) Elastic with surface topography; 2) Elastic with plane, free surface on top; 3) Viscoelastic with surface topography, where $Q = 10$ in the upper 10m, $Q = 15$ in the next 40m, and $Q = 30$ in the lower half–space – the Q–values are mutual for both P– and S–waves; and 4) Viscoelastic with plane, free surface on top and the Q–value distribution of 3). Figure 3 represents snapshots of scenarios 1)–4) above at time 2s, displaying the vertical particle velocity w along the vertical xz–section of the model at $y = 100$m (the middle of the y-dimension). The different snapshots of Figure 3 are scaled relative to each other, and so it is noteworthy to see how the low Q–values of the viscoelastic cases (Figures 3(c) and 3(d)) weaken amplitudes as well as greatly disperse waveforms compared to the exact same elastic cases (Figures 3(a) and 3(b)). The modest topographic elevation differences of only about 8m (Figure 2) do not cause large scattering effects however, as can be seen when comparing the elastic topography case (Figure 3(a)) with the plane surface case (Figure 3(b)), and to a lesser extent when comparing the viscoelastic topography case (Figure 3(c)) to its plane surface analogue (Figure 3(d)). After 2 seconds the clearest visible differences are a few wavefront disruptions in the topography cases. For the elastic cases, the topography causes some wavefront amplitude amplification - seen in particular at the right portion of Figure 3(a) when comparing with Figure 3(b). Some amplification from topography can also be seen in some of the isolated waveforms of the viscoelastic cases.

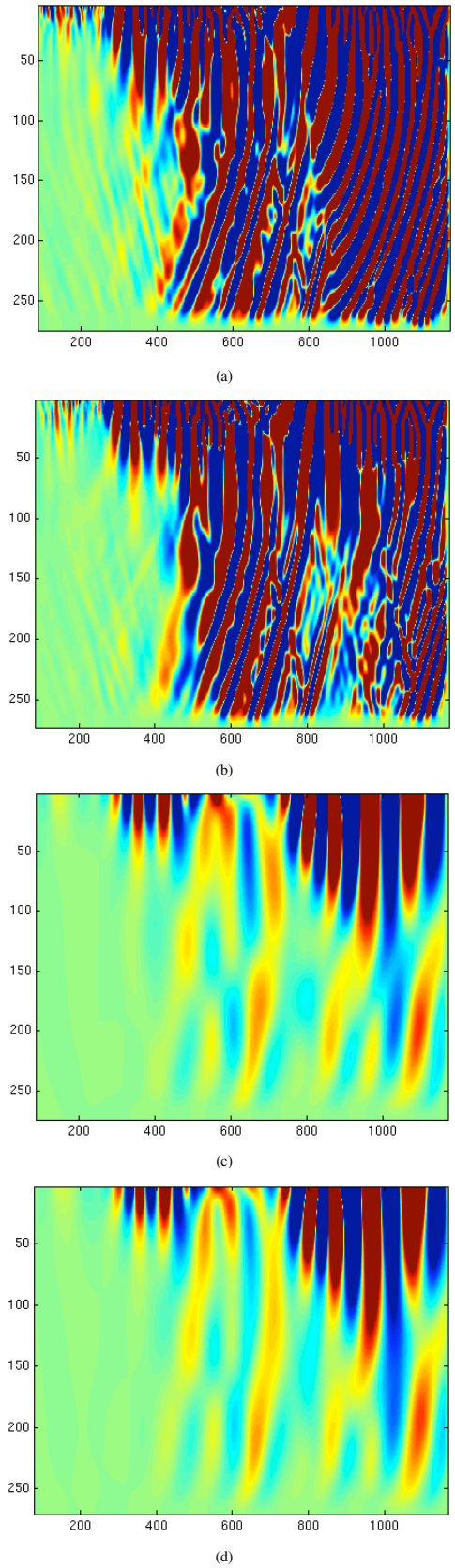

Figure 3: Vertical particle velocity snapshots at time 2 seconds along the vertical xz-plane of scenarios 1)–4) listed.

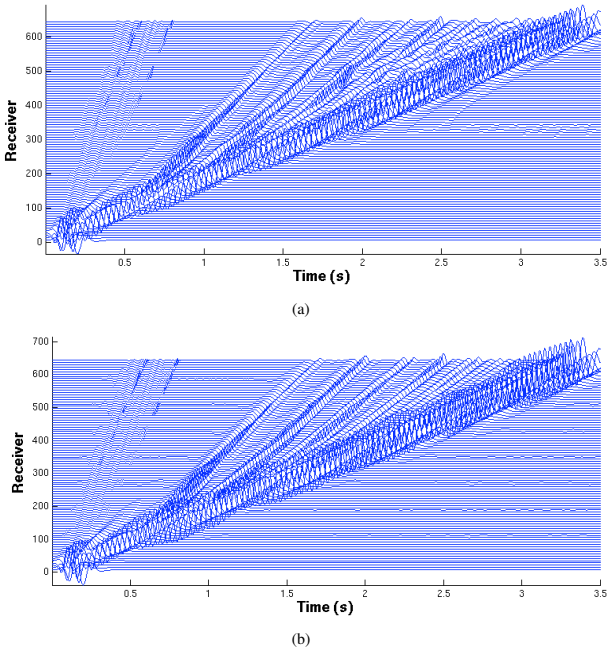

Figure 4: Pressure seismograms of scenarios 1) and 2) described. The 650 1m–spaced receivers are decimated by 7, to constitute 7m between each trace shown.

Pressure seismograms up to 3.5s are shown for scenarios 1)–4) in the two next figures. Figure 4 displays the two elastic simulations with (Figure 4(a)) and without (Figure 4(b)) topography, and although the two seismograms are similar, the wavefield is more broken up in the forward scattered field in the topography case after 1.5s simulation time. Even for this modest topography, a clear difference in the wavefields can be noted. There is precedence in the literature for this. Observations (Lee et al., 2009) show a teleseismic example in which scattering from topography is visible for elevation to S–wavelength ratio of 1:6. Due to the strong attenuation resulting from the low Q–values applied, the corresponding viscoelastic seismograms (Figure 5) has amplitudes enhanced by a factor 10 compared to Figure 4, and acts to downplay the importance of including topography in modeling of domains of high attenuation. Even the low–frequency Rayleigh (Rg) waves are attenuated to the extent of showing no significant scattering due to topography. When comparing the topography case (Figure 5(a)) with the plane surface case (Figure 5(b)), only a few broken–up waveforms around 1.5s are seen to be different before the medium attenuation causes the subsequent waveforms to decay in amplitude and to be very similar between the topography and no–topography cases.

CONCLUSIONS

We simulated a Ricker wavelet at the surface of a real 3D topography over a 2 1/2D medium, for elastic and real viscoelastic media to assess and isolate effects of free surface topography in each case. Elastic simulations reveal that even a modest topography of only 8m elevation differences have clear effects on the scattered wavefields after enough time, even when the central source S–wavelength is far greater than the typical elevation variation wavelength. Introducing the real viscoelastic layers however, downplays the importance of inclusion of this modest topography in simulations because even low–frequency scattering is greatly attenuated and almost negligible after enough time. For earlier simulation times however, we see some clear differences between free surface topography and plane surface results even in low–Q viscoelastic cases. Furthermore, in cases where elevation changes approach the S–wavelength, we anticipate the effect of topography will remain and become important in surface wave simulation and inversion.

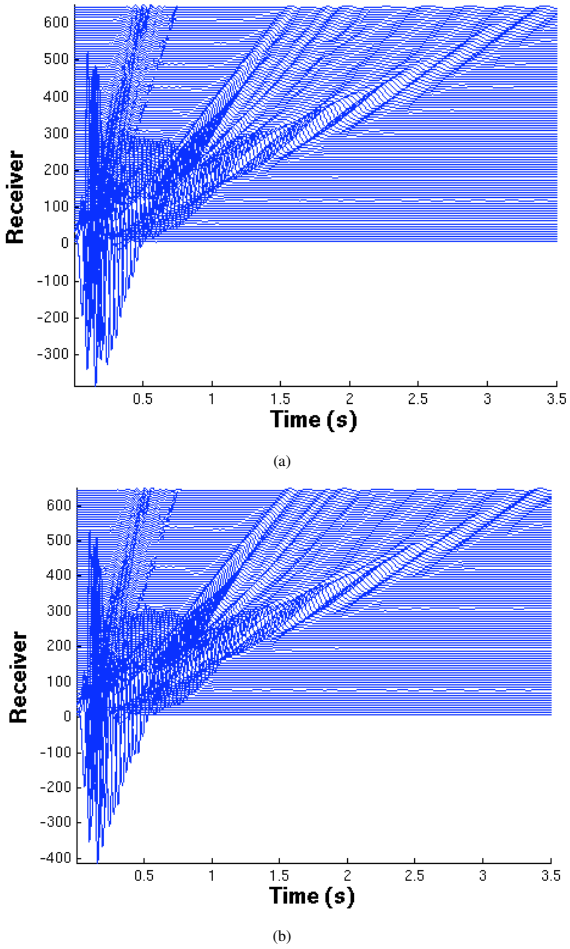

Figure 5: Pressure seismograms of scenarios 3) and 4) described. The 650 1m–spaced receivers are decimated by 7, to constitute 7m between each trace shown. Traces from the viscoelastic runs are enhanced by a factor 10 from the ones in Figure 4.

ACKNOWLEDGMENT

We acknowledge John Anderson, Sunwoong Lee and Anatoly Baumstein for preparing the model used in the experiments.

REFERENCES

Basabe, J. D. and M. Sen, 2007, Grid dispersion and stability criteria of some common finite-element methods for acoustic and elastic wave equations: Geophysics, **72**, T81–T95.

Blanch, J. O., J. O. A. Robertsson, and W. W. Symes, 1995, Modeling of a constant Q: Methodology and algorithm for an efficient and optimally inexpensive viscoelastic technique: Geophysics, **60**, 176–184.

Carcione, J. M., 1993, Seismic modeling in viscoelastic media: Geophysics, **58**, 110–120.

Carcione, J. M., D. Kosloff, and R. Kosloff, 1988, Wave propagation simulation in a linear viscoacoustic medium: Geophys. J. Roy. Astr. Soc., **93**, 393–407.

Cerjan, C., D. Kosloff, R. Kosloff, and M. Reshef, 1985, A nonreflecting boundary condition for discrete acoustic and elastic wave equations: Geophysics, **50**, 705–708.

Fornberg, B., 1988, Generation of finite difference formulas on arbitrary spaced grids: Mathematics of Computation, **51**, 699–706.

Hestholm, S. O., 1999, 3–D finite difference viscoelastic wave modelling including surface topography: Geophys. J. Int., **139**, 852–878.

Hestholm, S. O. and B. O. Ruud, 1998, 3–D finite difference elastic wave modeling including surface topography: Geophysics, **63**, 613–622.

———, 2002, 3D free–boundary conditions for coordinate–transform finite–difference seismic modelling: Geophysical Prospecting, **50**, 463–474.

Holberg, O., 1987, Computational aspects of the choice of operator and sampling interval of numerical differentiation in large–scale simulation of wave phenomena: Geophysical Prospecting, **35**, 629–655.

Kindelan, M., A. Kamel, and P. Sguazzero, 1990, On the construction and efficiency of staggered numerical differentiators for the wave equation: Geophysics, **55**, 107–110.

Komatitsch, D., C. Barnes, and J. Tromp, 2000, Wave propagation near a fluid-solid interface: A spectral-element approach: Geophysics, **65**, 623–631.

Komatitsch, D., F. Coutel, and P. Mora, 1996, Tensorial formulation of the wave equation for modelling curved interfaces: Geophys. J. Int., **127**, 156–168.

Komatitsch, D., J.-P. Vilotte, R. Vai, J. Castillo-Covarrubias, and F. Sánchez-Sesma, 1999, The spectral element method for elastic wave equations–applications to 2-d and 3-d seismic problems: International Journal for Numerical Methods in Engineering, **45**, 1139–1164.

Lee, S. and W. S. Ross, 2008, 3D mitigation of surface–wave noise in spatially inhomogeneous media: SEG International Exposition and 78th Annual Meeting, San Antonio, Expanded Abstracts, 2561–2566, Society of Exploration Geophysicists.

Lee, S.-J., D. Komatitsch, B.-S. Huang, and J. Tromp, 2009, Effects of topography on seismic wave propagation: An example from northern taiwan: Bull. Seism. Soc. Am., **99**, 314–325.

Tessmer, E. and D. Kosloff, 1994, 3–D elastic modeling with surface topography by a Chebychev spectral method: Geophysics, **59**, 464–473.

Tessmer, E., D. Kosloff, and A. Behle, 1992, Elastic wave propagation simulation in the presence of surface topography: Geophys. J. Int., **108**, 621–632.